Journal of
Applied Crystallography

ISSN 0021-8898

Received 17 December 2003
Accepted 23 February 2004

© 2004 International Union of Crystallography
Printed in Great Britain – all rights reserved

First results of digital topography applied to macromolecular crystals

Jeffrey J. Lovelace,[a] Alexei S. Soares,[b] Henry D. Bellamy,[c] Robert M. Sweet,[b] Edward H. Snell[d] and Gloria E. O. Borgstahl[a]*

[a]Eppley Institute for Cancer Research, 987696 Nebraska Medical Center, Omaha, NE 68198-7696, USA, [b]Biology Department, Brookhaven National Laboratory, Upton, NY 11973, USA, [c]CAMD/LSU, 6980 Jefferson Hwy, Baton Rouge, LA 70806, USA, and [d]NASA Laboratory for Structural Biology, Code SD46, NASA MSFC, Huntsville, AL 35812, USA. Correspondence e-mail: gborgstahl@unmc.edu

An inexpensive digital CCD camera was used to record X-ray topographs directly from large imperfect crystals of cubic insulin. The topographs recorded were not as detailed as those which can be measured with film or emulsion plates, but do show great promise. Six reflections were recorded using a set of finely spaced stills encompassing the rocking curve of each reflection. A complete topographic reflection profile could be digitally imaged in minutes. Interesting and complex internal structure was observed by this technique. The CCD chip used in the camera has anti-blooming circuitry and produced good data quality, even when pixels became overloaded.

1. Introduction

Topography is the high-spatial resolution imaging of a Bragg reflection and is used to reveal the individual parts of the crystal that contribute to the reflection. Topography provides detailed insight into the diffraction properties and quality of a crystal (Fourme *et al.*, 1995; Stojanoff & Siddons, 1996; Stojanoff *et al.*, 1996, 1997; Dobrianov *et al.*, 1998; Otálora *et al.*, 1999; Boggon *et al.*, 2000). Contrast in a reflection topograph is produced by irregularities in the lattice, *e.g.* from defects or domain boundaries. By quantifying topographic data, one can compare the diffraction properties of different crystals in detail. High-resolution images of reflections are typically acquired with fine-grain X-ray sensitive film (typically 2–3 μm grain size) and, less often, with nuclear emulsion plates (1 μm). Drawbacks to the use of film or emulsion plates include slow processing time, variation between batches and processing chemicals, limited dynamic range, and the extra digitization step. Repeatable high-accuracy quantitative analysis with these techniques is difficult and time consuming. Film and, to a lesser extent, emulsion plate processes are slowly being replaced with digital equivalents in many fields. In this study, we explored the use of an inexpensive charge-coupled device (CCD) camera with 8 μm pixels to capture topographic images directly from macromolecular crystals.

2. Experimental setup and data processing

The CCD topography system was based on an Electrim Corporation EDC-2000S camera, which uses a Texas Instruments TI-TC281 CCD chip. For this experiment, Texas Instruments provided us with a TI-TX281-31 CCD, which was a TC281 with the cover glass removed. The TC281 has an 8 × 8 mm active area enclosing a 1000 × 1000 array of 8 μm square pixels. The pixel well capacity is 32000 electrons. For CCDs, there is a trade off between pixel size and well capacity, with smaller pixels having a smaller well capacity. The CCD incorporates anti-blooming circuitry. Blooming in a CCD occurs when the charge accumulating in a pixel overflows into neighboring pixels. With anti-blooming, spatial resolution is preserved and intensity information is lost in pixels that overflow. The preservation of spatial resolution at the expense of precise intensity data is a suitable compromise for digital topography. The EDC-2000S camera offers software-programmable adjustment of the gain, offset and exposure time.

For data collection, NSLS Beamline X26-C was configured for parallel radiation by taking the focusing mirror out of the beam path. The beamline parameters were approximately 0.001° and 0.0025° for the vertical and horizontal beam divergences, respectively, and $\Delta\lambda/\lambda$ was 2.00×10^{-4}. The wavelength was 1.52 Å. Fig. 1(*a*) shows the (4 + 2)-circle diffractometer used to position the crystal and the detector. The assignments of the motor axes differ from conventional Eulerian cradle geometries typically used, so they are shown in Figs. 1(*b*)–1(*d*). In an effort to simulate a conventional setup, the ω axis was held stationary so that the ψ axis was held horizontal and perpendicular to the X-ray beam. The axes φ and χ were used to position the reflections so that they were directly above the beam in order to minimize the effect of beam divergence and Lorentz broadening on the reflection profile (Bellamy *et al.*, 2000). The 2θ and ν motions were used to position the detectors. After a reflection was located with the scintillation counter, the topography camera was inserted in front of the scintillation counter as shown in Fig. 1(*e*). The camera and the X-ray shutter were synchronized manually; the camera exposure was 10 s and the X-ray shutter time was 5 s.

Two large cubic insulin crystals (> 500 × 500 μm) that might provide topographs with prominent features were selected (Fig. 2). Sequences of topographic images were collected on six different reflections (Table 1) with two reflections from crystal A (Fig. 3*a*) and four from crystal B (Fig. 3*b*). The data collection parameters are detailed in Table 1. The sequences were collected as a series of stills separated by incremental rotations about the ψ axis (Fig. 1). Reflection intensity profiles about the ψ axis were also collected with a scintillation counter for each of the four reflections from crystal B.

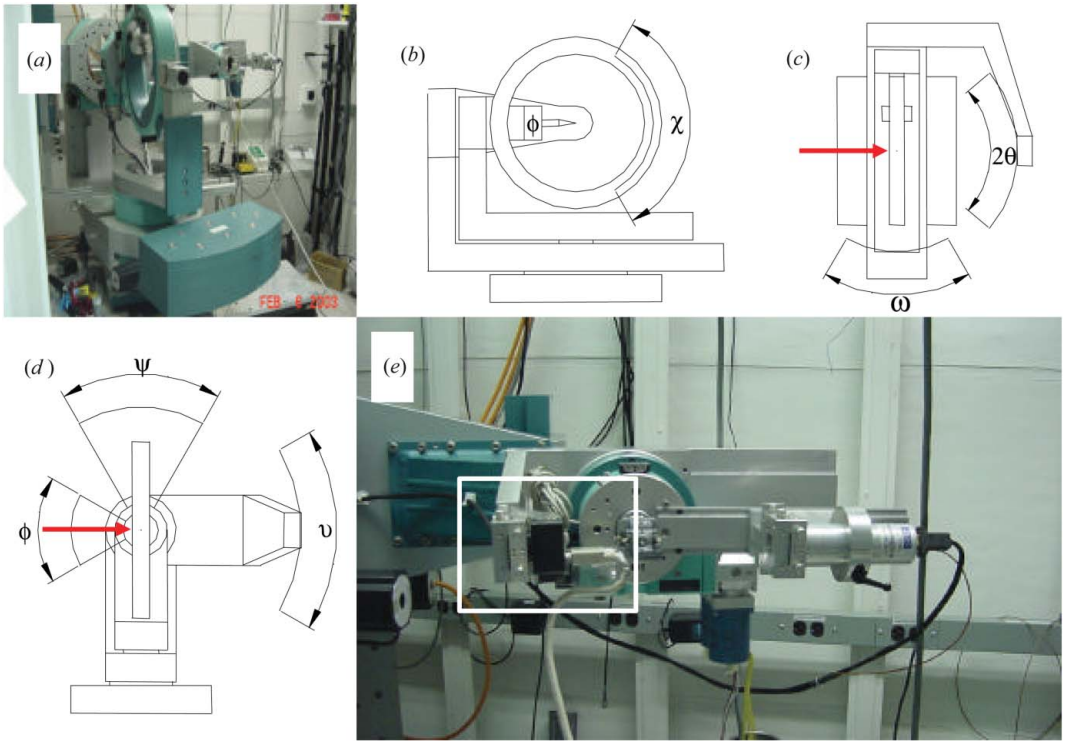

Figure 1
Experimental setup. (*a*) Wide-angle view of the diffractometer with the CCD and scintillation counter installed. (*b*) Diagram of the beam view of the diffractometer with the χ and φ motions labelled. (*c*) Top view of the diffractometer with the 2θ and Ω motions labelled. (*d*) Side view of the diffractometer with the φ, ψ and υ motors labelled. The red arrow indicates the X-ray beam location and direction. (*e*) Close-up view of the CCD camera and scintillation counter (inside white box). A custom-sized length of clear single-sided bonding strip was used to hold the CCD camera firmly in front of the scintillation counter.

The images were recorded using a software package we developed, called *Ripple*. Currently, *Ripple* performs a limited set of operations, but the eventual goal is to develop a unified image-collection and processing platform. The images are written to disk in TIFF format (Aldus Corporation, 1986), which allows image-processing concepts to be prototyped and analyzed with *MATLAB* (The Math Works Inc., 1992).

The raw data images from the camera were passed through a seven-step processing sequence to improve the images (see Figs. 4 and 5). The raw image acquired from the CCD showed excellent signal for the reflection topograph (Fig. 4*a*). The first step was to remove the dark current noise by subtracting a dark-current (no X-rays) image of equal exposure time (Fig. 4*b*). The TC-281 CCD was designed for use in short exposure time environments ($\ll 1$ s) and has a significant dark current when the exposure time is of the order of seconds, as it was in this case. This could be reduced by cooling the CCD. The second step was to reduce the electrical ripple noise that is present on the image (shown in Fig. 5*a*). An image processing tool known as a wavelet transform was used to reduce the ripple noise. The original image was decomposed one level with the sixth-order Daubechies wavelet using the discrete wavelet transform (Daubechies, 1992). Most of the complex noise appeared in one of the sub-bands. By removing the sub-band containing the noise and applying the inverse discrete wavelet transform to the remaining sub-bands, the result was a more evenly distributed background with lower overall intensity and less structure (Fig. 5*b*). This correction was carried out over the entire surface of the CCD image but had little effect on the region where the reflection was located (Figs. 4*b* and 4*c*). For the third step, a histogram cut-off filter was used to remove the remaining background noise from the image and leave the intensity near the reflection. The histogram filter found the average and standard deviation of all pixels and then set each pixel to zero that had a value less than the mean plus 2.5 standard deviations (Fig. 4*d*). The fourth step was to apply a median filter to clean up the speckle nature of the data (Fig. 4*e*). The median filter replaced the value of each pixel with the median value of a box of surrounding pixels. The fifth step was to use the inverse discrete wavelet transform (Strang & Nguyen, 1996; Mallat, 1998) to enhance the resolution and smooth the image (Fig. 4*f*; see also the zoomed-in regions in Figs. 4*e* and 4*h*). The sixth step was to use a histogram-cut-off filter and clean out any remaining low-level noise (Fig. 4*g*). The same method as in the fourth step was used. The final seventh step was to expand and digitize the data back into the integer range 0 to 255, by examining the entire sequence and using the maximum and minimum values to scale all the images in the sequence (Fig. 4*h*). The color table used in all of the reflection images has level zero as white and then levels 1 through 255 (Fig. 4, bottom) going from blue to red. Using white as level zero

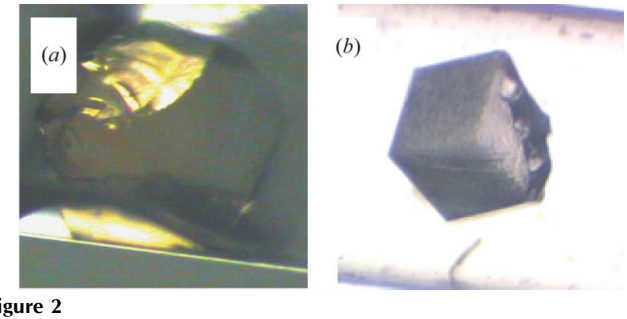

Figure 2
Visible-light micrographs of specimen crystals. (*a*) After-exposure image of crystal A. Its coloration was yellow, indicating large amounts of radiation damage. (*b*) After-exposure image of crystal B.

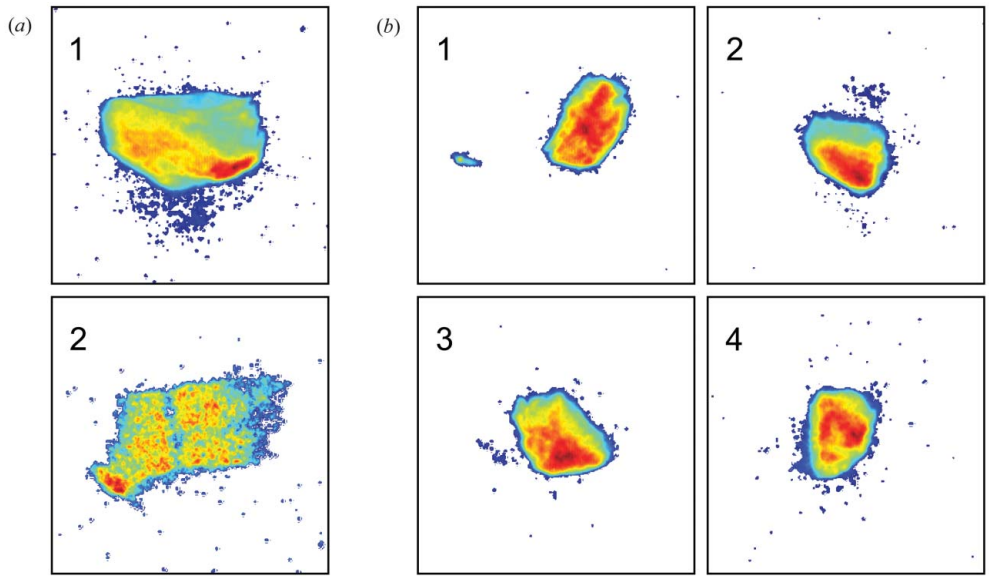

Figure 3
The integrated intensity of combining all of the images for each of the reflections. (*a*) Results for reflections 1 and 2 from crystal A. (*b*) Results for reflections 1, 2, 3 and 4 from crystal B.

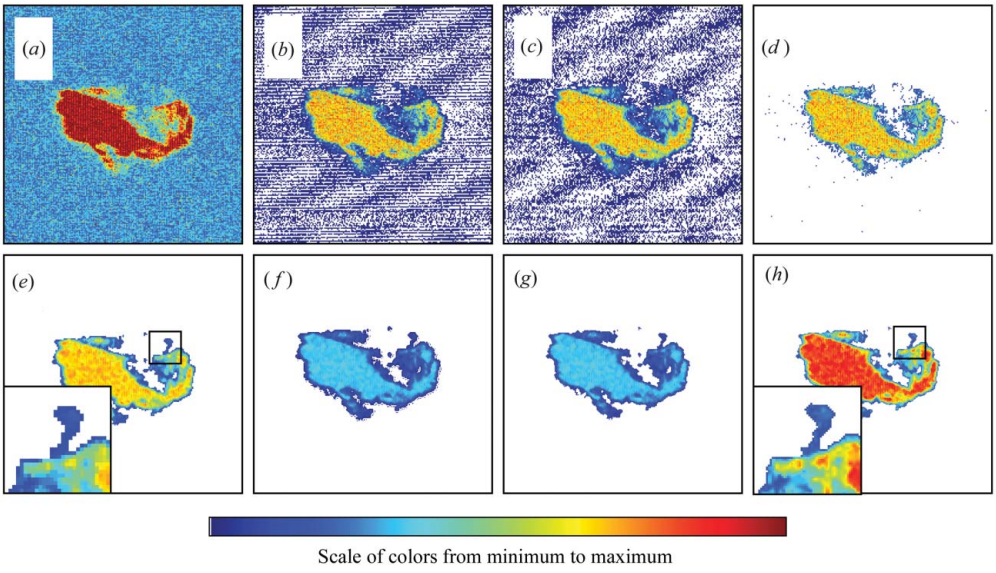

Figure 4
Image processing example. (*a*) Raw image. (*b*) Dark-current-subtracted image. (*c*) Wavelet-transform-filtered image. (*d*) Histogram-filtered image. (*e*) Median filtered image. (*f*) Wavelet-resolution-enhanced image. (*g*) Histogram-filtered image. (*h*) Intensity-scaled image. The boxes in (*e*) and (*h*) show the effects of the resolution enhancement.

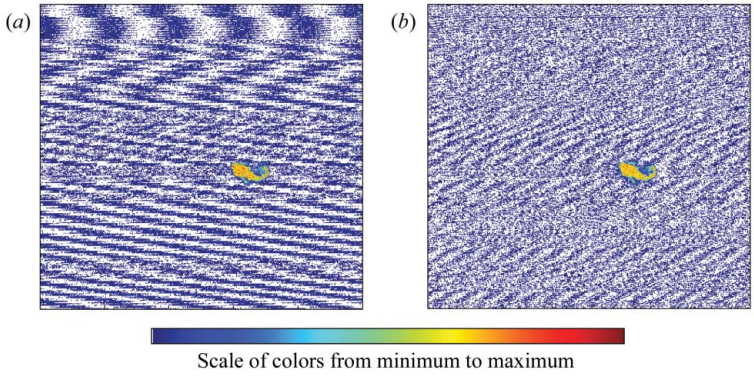

Figure 5
Reduction of ripple noise with the wavelet transform. (*a*) Raw image with dark-current subtracted. (*b*) Image after wavelet processing.

shows how well the processing was able to eliminate the noise from the background, while the strong signal and detailed shape of the reflection topograph remains the same (compare Figs. 4*a* and 4*h*).

3. Results

The two crystals, A and B, used for data collection are shown in Figs. 2(*a*) and 2(*b*), respectively. Both photographs were taken after the experiment. The post-experimental picture of crystal A has a yellowish tint, which suggests there was significant radiation damage, whereas that of crystal B shows no yellowish tint, indicating that it suffered less radiation damage than crystal A.

Many excellent topographs were quickly measured. For each of the six Bragg reflections studied, 32 to 64 topographic images were measured sequentially (Table 1). Summation of all of the images in a sequence shows the three-dimensional shape and orientation of the crystals for each of the six reflections (Fig. 3). Areas of the crystal that stayed in a diffracting condition for many frames are red and areas that diffracted briefly are blue. Selected individual images for each reflection show the regions in diffraction condition for each ψ step (Fig. 6).

For crystal A, two days of radiation damage occurred between topographic imaging of reflections 1 and 2 as this crystal had been used for another unrelated experiment during the day-shift at the synchrotron (Fig. 3*a*). The reflections are unrelated and the crystal was in random orientations for data collection. There are several interesting observations for these two reflections (Figs. 3*a*1 and 3*a*2). The first is that there appears to be an area of the crystal that stayed in diffracting condition for a longer amount of time in both reflections (indicated by bright red). In reflection 1, the crystal appears as a box with a red nodule on the right-side face, and in reflection 2, a side view, with the red nodule on the far lower left end. Reflection 2 also appears to

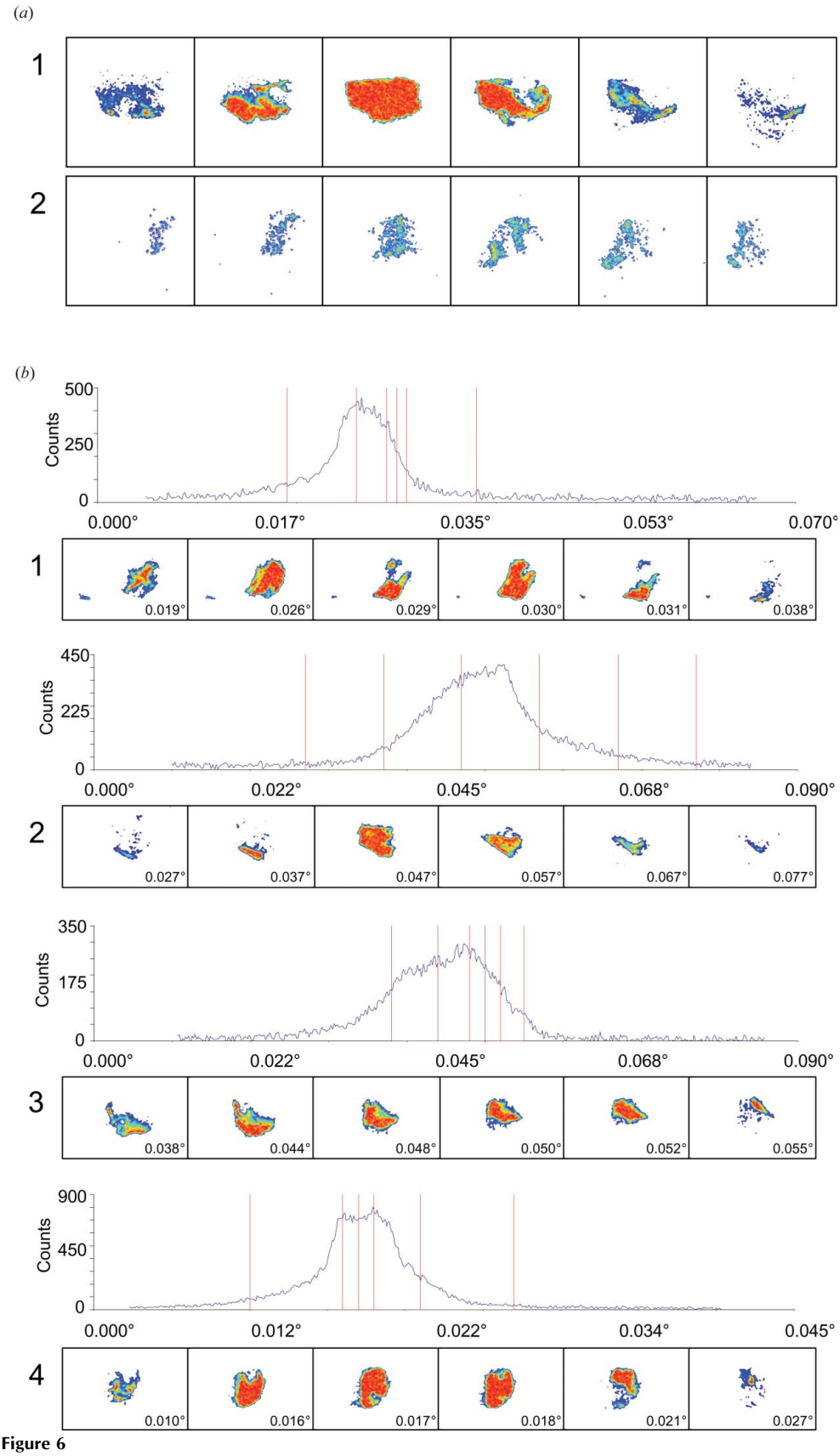

Figure 6
Topographic sequences for reflections from crystals A and B. (*a*1) Evenly spaced sequence from reflection 1 of crystal A. (*a*2) Evenly spaced sequence from reflection 2 of crystal A. (*b*1)–(*b*4) Interesting images from the topography study of crystal B with the associated intensity profiles recorded with the scintillation counter for reflections 1–4, respectively. The red lines indicate where each frame was taken sequentially from left to right.

be composed of three large diffracting domains, two smaller ones on the right side and a larger one on the left, with a small gap of almost no diffraction dividing those areas. When comparing the sequences, Figs. 6(*a*1) and 6(*a*2), another observation is that the images are significantly degraded between reflection 1 and 2, with reflection 2 being much more speckled and of lower intensity. This could be due to several factors, including radiation damage, dehydration and the possibility that this reflection normally has a weaker intensity with poorer counting statistics.

Crystal B was used exclusively for topography measurements. All of the measured reflections for crystal B were well defined and the signal was significantly above background (Fig. 3*b*). The selected individual images from crystal B (Fig. 6*b*) also show the associated reflection profiles, integrated intensity *versus* ψ step, which were measured with a scintillation counter. For crystal B, reflection 1, there was a small satellite reflection that appeared off to the left-hand side (Fig. 3*b*1). Although its intensity is much weaker, it was clearly visible in the raw images and existed only on frames where the reflection was diffracting (Fig. 6*b*1). The topography of crystal B was much more complex than that of crystal A. It had sharp transitions between areas of the crystal that were diffracting during the rotation instead of the smooth transitions seen in crystal A. Some of the rapid transitions occurred over about 0.001°. These transitions are highlighted in Figs. 6(*b*1), 6(*b*3) and 6(*b*4).

4. Conclusions

The topographs recorded here were not as detailed as those recorded with film or nuclear emulsions but do show great promise. Spatial resolution is a key parameter in topography and the CCD with 8 µm pixel size provided spatially resolved data on the crystals in this case. A useful feature of the CCD was the anti-blooming circuitry which gave sharp detail between

regions of the crystal, even when adjacent pixels were overloaded. In a CCD without this capability, overloading would have led to the corruption of neighboring pixels.

In a previous study, a CCD-based X-ray camera was used to study topography of synthetic diamonds (Ludwig *et al.*, 2001). A powder phosphor was used to convert the X-rays to visible light and a fibre-optic face-plate to channel the visible light to the chip surface for detection. We used the CCD to detect X-rays directly. Although the sensitivity of the CCD for X-rays was diminished by not using a phosphor coating, the high resolution afforded by the small pixel size of the CCD was retained. Phosphor coating would blur the topographic image by increasing the point spread function of the detector. We had expected radiation damage of the CCD to be a problem (hence the use of an inexpensive CCD), but the CCD proved to be fairly resistant to X-rays. A direct beam test exposure, admittedly with a fairly low-intensity parallel synchrotron beam, caused no detectable damage as judged by subsequent images. A more expensive CCD, with an even smaller pixel size, is justified for these studies.

The CCD camera was able to image relatively weak X-ray reflections from a macromolecular crystal without the need for a phosphor coating. The resolution of the particular CCD used was adequate to see complex structure within the reflection. Once a reflection was located, a topograph for an individual reflection could be acquired in a matter of seconds. A complete topographic reflection profile could be acquired in less than 15 min, depending on the number of images required. This is a huge improvement over film and the speed could be further increased by improved integration of the CCD and goniostat control systems. The CCD appeared to suffer no serious radiation damage and there were no areas of the CCD rendered unusable after this experiment. Digital topography will enable the use of the topography technique as a quantitative analysis method for macromolecular crystals

Data for this study were measured at beamline X26-C of the National Synchrotron Light Source. Financial support comes principally from the National Center for Research Resources of the National Institutes of Health, and from the Offices of Biological and Environmental Research and of Basic Energy Sciences of the US Department of Energy. The authors would like to thank Annie Héroux for extensive help at the beamline and Pixar for useful terminology. NASA Grant NAG8-1825 supported this work. EHS is a contractor to NASA through BAE SYSTEMS Analytical Solutions.

Table 1
Topography reflection list.

Reflection	Crystal	Resolution (Å)	Start ψ (°)	X-ray exposure time (s)/ integration time (s)	Step size (°)	Image count
1	1	9.8	NA	5/10	0.002	64
2	1	5.0	NA	10/10	0.002	35
3	2	6.7	6.520	5/10	0.001	32
4	2	6.7	6.480	5/10	0.001	61
5	2	6.5	6.820	5/10	0.001	41
6	2	6.6	6.795	5/10	0.001	46

References

Aldus Corporation (1986). *TIFF Revision 6.0*, Mountain View, CA.
Bellamy, H. D., Snell, E. H., Lovelace, J., Pokross, M. & Borgstahl, G. E. O. (2000). *Acta Cryst.* D**56**, 986–995.
Boggon, T. J., Helliwell, J. R., Judge, R. A., Olczak, A., Siddons, D. P., Snell, E. H. & Stojanoff, V. (2000). *Acta Cryst.* D**56**, 868–880.
Daubechies, I. (1992). Ten lectures on wavelets. Philadelphi, PA.
Dobrianov, I., Finkelstein, K. D., Lemay, L. G. & Thorne, R. E. (1998). *Acta Cryst.* D**54**, 922–937.
Fourme, R., Ducruix, A., Riess-Kautt, M. & Capelle, B. (1995). *J. Synchrotron Rad.* **2**, 136–142.
Ludwig, W., Cloetens, P., Hartwig, J., Baruchel, J., Hamelin, B. & Bastie, P. (2001). *J. Appl. Cryst.* **34**, 602–607.
Mallat, S. G. (1998). *A Wavelet Tour of Signal Processing*. San Diego: Academic Press.
Otálora, F., García-Ruiz, J. M., Gavira, J. A. & Capelle, B. (1999). *J. Crystal Growth*, **196**, 546–558.
Stojanoff, V. & Siddons, D. P. (1996). *Acta Cryst.* A**52**, 498–499.
Stojanoff, V., Siddons, D. P., Monaco, L. A., Vekilov, P. & Rosenberger, F. (1997). *Acta Cryst.* D**53**, 588–595.
Stojanoff, V., Siddons, D. P., Snell, E. H. & Helliwell, J. R. (1996). *Synchrotron Rad. News*, **9**, 25–26.
Strang, G. & Nguyen, T. (1996). *Wavelets and Filter Banks*. Cambridge: Wellesley Cambridge Press.
The Math Works Inc. (1992). *MATLAB Reference Guide*, Natick, MA.